Computational Mechanics 17 (1995) 151–168 © Springer-Verlag 1995

On the feasibility of using smoothed particle Hydrodynamics for underwater explosion calculations

J. W. Swegle, S. W. Attaway

Abstract SPH (Smoothed Particle Hydrodynamics) is a gridless Lagrangian technique which is appealing as a possible alternative to numerical techniques currently used to analyze high deformation impulsive loading events. In the present study, the SPH algorithm has been subjected to detailed testing and analysis to determine the feasibility of using PRONTO/SPH for the analysis of various types of underwater explosion problems involving fluid-structure and shock-structure interactions. Of particular interest are effects of bubble formation and collapse and the permanent deformation of thin walled structures due to these loadings. These are exceptionally difficult problems to model. Past attempts with various types of codes have not been satisfactory. Coupling SPH into the finite element code PRONTO represents a new approach to the problem. Results show that the method is well-suited for transmission of loads from underwater explosions to nearby structures, but the calculation of late time effects due to acceleration of gravity and bubble buoyancy will require additional development, and possibly coupling with implicit or incompressible methods.

1 Introduction

SPH (Smoothed Particle Hydrodynamics) [Lucy (1977), Gingold and Monaghan (1982), Monaghan (1982, 1985, 1988), Cloutman (1990a, 1990b), Benz (1990), Swegle, Attaway, Heinstein, Mello, and Hicks (1994), Swegle, Attaway, and Hicks (1995)] is a gridless Lagrangian technique which is appealing as a possible alternative to numerical techniques currently used to analyze high deformation impulsive loading events, such as hypervelocity impact or explosive loading of materials. While Eulerian techniques can easily handle the gross motions associated with the large deformations involved in such events, detailed analysis is difficult because of the lack of history and the smearing and spreading of information (referred to here as diffusion) as the mass moves through the fixed-in-space Eulerian grid. Standard Lagrangian techniques, although desirable due to their ability to keep accurate histories of the events associated with each Lagrangian element, cannot be used because the material deformations are so large that the Lagrangian grid becomes severely distorted and the calculation breaks down.

SPH offers a possible solution to these difficulties. The technique is Lagrangian and thus provides complete history information and should be well-suited for tracking details of the deformation process associated with each material element. SPH is actually quite similar to standard Lagrangian methods. In fact, the term hydrodynamic in the name is a misnomer, since strength is easily included. The difference from standard techniques is that spatial gradients are approximated by a method which is applicable to an arbitrary distribution of interpolation points so that no grid is required. Thus, the technique is gridless and should be applicable to arbitrary deformations. The lack of a grid also means that 3D calculations are as easy as 1D. Various organizations which have chosen SPH as a natural technique for large deformation calculations have used it to produce numerous results and are strongly supportive of its capabilities.

SPH has been coupled into the transient dynamics finite element code, PRONTO [Taylor and Flanagan (1987)], providing a combined capability which exceeds the individual capabilities of either method. The coupling embeds the SPH method within the finite element code and treats each SPH particle as a different element type within the finite element architecture. Contact surface algorithms used in the finite element method are used to couple the SPH particles with the finite elements. The ability to couple particle methods and finite element methods allows fluid-structure interaction problems to be solved efficiently. SPH can be used in large deformation regions where standard Lagrangian finite elements would become too distorted. However, SPH need not be used for the entire problem. Low deformation regions and structures can be treated with finite elements. Also, very thin regions can be treated with shell elements. Since various types of boundary conditions are easier to apply to finite elements than SPH, SPH regions can be surrounded by finite elements for the purpose of applying boundary conditions.

The purpose of the present effort is to evaluate the feasibility of using PRONTO/SPH for the analysis of various types of underwater explosion problems involving fluid-structure and shock-structure interactions. Of particular interest are effects of bubble formation and collapse such as the loads on structures due to bubble pulses and cavitation closure, the formation of re-entrant jets during bubble collapse, the interaction of these jets with a structure, and the permanent deformation of thin

Communicated by S. N. Atluri, 30 May 1995

J. W. Swegle, S. W. Attaway
Material and Structural Mechanics Department, 1518 Sandia National Laboratories Albuquerque, New Mexico 87185, USA

Correspondence to: J. W. Swegle

This work was performed at Sandia National Laboratories, which is operated for the U.S. Department of Energy under Contract No. DE-AC04-94AL85000, and was partially funded by the Naval Surface Warfare Center under WFO proposal # 15930816

walled structures due to these loadings. These are exceptionally difficult problems to model. Past attempts with various types of codes have not been satisfactory. Coupling SPH into the finite element code PRONTO represents a new approach to the problem.

As part of this effort, considerable development work has been done on PRONTO/SPH. SPH has been added to the three-dimensional version of PRONTO, including the latest developments in variable smoothing length, methods for calculating density, as well as interface and smoothing options. Also, an axisymmetric option has been added to the two-dimensional version of PRONTO. The next section provides a review of the SPH method. The reader should consult Swegle, Attaway, Heinstein, Mello, and Hicks (1994) for a thorough description of SPH and its coupling into PRONTO.

2
SPH description

The basic objective of the SPH method is the numerical solution of the initial-boundary value problem defined by the partial differential equations which express the laws of conservation of mass, momentum, and energy, plus constitutive relations describing the materials in the problem. It is called an initial-boundary value problem because additional information is required which consists of 1) initial values for all variables at all positions at time zero and 2) boundary values for all variables at the boundary positions at all times. The task is to extend this information to all positions and times of interest. The primary difference between the smoothed particle method and standard Lagrangian finite-difference techniques is the replacement of grid-based approximation of spatial derivatives with a technique applicable to a random collection of interpolation points. In order to appreciate this difference, consider the following brief sketch of the general steps associated with any explicit numerical method:

1. Discretize information in time and space so that it is only known at a discrete number of positions and times. Start the cycle with the information at all positions known at time t. This may be either time zero at which all information was initially defined, or some later time to which the information has been advanced.
2. Based on the values of the stresses at each discretized location at time t, construct an approximation to the stress divergence. The acceleration of each discretized location at time t can then be computed from the law of conservation of momentum (the equation of motion).
3. Use the accelerations at time t to compute the new velocities and finally the new positions at time $t + \Delta t$, where Δt is the incremental time step. Calculate the new strain rates from the spatial derivatives of the new velocities, and the new strains from the new positions.
4. Use the new strains and strain rates to calculate the new stresses at time $t + \Delta t$. All information has now been advanced to the new time, and the cycle can be repeated.

During this process, spatial derivatives of stress are required to compute accelerations, and spatial derivatives of velocity are required to compute strain rates. It is in this step that SPH differs from standard grid-based Lagrangian methods. The grid-based methods assume a fixed connectivity between particles (neighbors are assumed to remain neighbors) in order to construct approximations for spatial derivatives, while SPH uses the Kernel approximation, which is based on randomly distributed interpolation points with no assumptions about which points are neighbors. SPH is thus applicable to large deformations while grid-based Lagrangian techniques are not. Details are provided below.

2.1
Kernel approximation

Consideration of standard Lagrangian finite-difference techniques shows that the major purpose of the spatial grid is to provide a basis for the construction of approximations to spatial derivatives. As shown in Fig. 1, the grid provides a framework which specifies the relationship between the various nodes and allows algorithms for estimating spatial derivatives to be implemented. For instance, a standard two-dimensional finite-difference approximation [Swegle (1978)] for the partial derivative with respect to x at point P is

$$\left.\frac{\partial \psi}{\partial x}\right|_P \approx \left(\oint_{C_{1234}} \psi\, dy\right) / A_{1234} \approx \frac{(\psi_1 - \psi_3)(y_2 - y_4) + (\psi_2 - \psi_4)(y_1 - y_3)}{2A_{1234}}, \tag{2.1}$$

where the approximation is obtained by applying Green's theorem in the plane and taking the line integral around the quadrilateral surrounding the point P, with A_{1234} the area of the quadrilateral. The problem with this technique is that it assumes that the same four nodes will always surround point P. Also, as the grid distorts and the quadrilateral becomes less square, the approximation loses accuracy.

The smoothed particle technique involves replacing grid-based approximations such as Eq. (2.1) with algorithms applicable to an arbitrary collection of interpolation points. The basis of the method is the kernel estimate, which starts from the identity

$$f(\boldsymbol{x}) = \int f(\boldsymbol{x}')\,\delta(\boldsymbol{x} - \boldsymbol{x}')\,d\boldsymbol{x}', \tag{2.2}$$

where f is a vector function of the three-dimensional position vector $\boldsymbol{x}$, $d\boldsymbol{x}'$ is a volume, and $\delta(\boldsymbol{x} - \boldsymbol{x}')$ is the Dirac delta function. If $\delta(\boldsymbol{x} - \boldsymbol{x}')$ is replaced by a kernel function $W(\boldsymbol{x} - \boldsymbol{x}', h)$ where h is known as the smoothing length, the result is the kernel estimate

$$f(\boldsymbol{x}) \approx \int f(\boldsymbol{x}')\, W(\boldsymbol{x} - \boldsymbol{x}', h)\, d\boldsymbol{x}'. \tag{2.3}$$

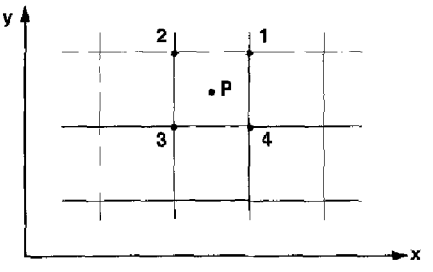

Fig. 1. Standard finite-difference grid

Various possibilities exist for the choice of $W(x-x')$. The requirements that are usually placed on the kernel function are 1) it reduces to the delta function,

$$\lim_{h\to 0} W(x-x',h)=\delta(x-x'), \tag{2.4}$$

2) it is normalized,

$$\int W(x,h)\,dx=1, \tag{2.5}$$

and 3) it has compact support (is zero everywhere but on a finite domain),

$$W(x,h)=0 \quad \text{for} \quad |x|\geqq 2h. \tag{2.6}$$

The approximation for spatial derivatives is obtained by substituting $\nabla\cdot f(x)$ for $f(x)$ in Eq. (2.3),

$$\nabla\cdot f(x)\approx\int\nabla\cdot f(x')\,W(x-x',h)\,dx'. \tag{2.7}$$

The divergence in the integral is taken with respect to the primed coordinate system. Now

$$\nabla\cdot f(x')\,W(x-x',h)=\nabla\cdot(f(x')W(x-x',h)) -f(x')\cdot\nabla W(x-x',h) \tag{2.8}$$

so that

$$\nabla\cdot f(x)\approx\int\nabla\cdot(f(x')W(x-x',h))\,dx' -\int f(x')\cdot\nabla W(x-x',h)\,dx'. \tag{2.9}$$

The first term on the right side of the equation can be converted by means of the divergence theorem into an integral over the surface of the domain of integration

$$\int\nabla\cdot(f(x')W(x-x',h))\,dx'=\int_S f(x')W(x-x',h))\cdot\hat{n}\,dS=0. \tag{2.10}$$

The fact that the surface integral is zero follows from Eq. (2.6), as long as the region of integration is further than $2h$ from the boundary of the material. If it is not, modifications should be made to account for boundary conditions, although this is rarely done due to the fact that the unmodified method works for free surfaces. Thus,

$$\nabla\cdot f(x)\approx-\int f(x')\cdot\nabla W(x-x',h)\,dx'. \tag{2.11}$$

Again, all gradients in the above integrals are taken with respect to the primed coordinate system. The kernel approximation thus allows spatial gradients to be determined from the values of the function and the derivative of the kernel, rather than the derivatives of the function itself. A final step is to convert from continuous volume integrals to sums over discrete interpolation points. Note

$$\int\phi(x')\,dx'=\int\left(\frac{\phi(x')}{\rho}\right)\rho\,dx'. \tag{2.12}$$

If $\rho dx'$ is interpreted as the mass associated with the interpolation point and the integral is approximated by finite sums using the value of the integrand at the interpolation point, then

$$\int\phi(x')\,dx'\approx\sum_{J=1}^{N}\frac{\phi(x^J)}{\rho^J}m^J, \tag{2.13}$$

where the superscript indicates the value of the quantity at interpolation point J, and the sum is over N interpolation points. Thus, Eqs. (2.3) and (2.11) become

$$f(x)\approx\sum_{J=1}^{N}\frac{m^J}{\rho^J}f(x^J)W(x-x^J,h) \tag{2.14}$$

and

$$\nabla\cdot f(x)\approx-\sum_{J=1}^{N}\frac{m^J}{\rho^J}f(x^J)\cdot\nabla W(x-x^J,h), \tag{2.15}$$

where the gradient ∇W in Eq. (2.15) is with respect to x^J. The above equations provide continuous approximations to a function and its spatial gradient based on an arbitrary set of discrete interpolation points at which the function is known. It is clear from the above that SPH 'particles' should be thought of as interpolation points rather than as interacting mass elements. No connectivity or spatial relation of the points is assumed. The sum is over the entire set of points, although only those within the range of the kernel function (typically $2h$) will contribute. In order to avoid an N^2 algorithm in which the distance between all particles is tested to determine which particles contribute to the sums, a search algorithm is used to find neighbors.

Equation (2.15) provides a straightforward approximation for any spatial gradients which may be required in implementing the smoothed particle algorithm. However, variants of this relation are sometimes used which start either from the identity

$$\nabla\cdot f(x)=\frac{1}{\rho}[\nabla\cdot(\rho f(x))-f(x)\cdot\nabla\rho] \tag{2.16}$$

or

$$\nabla\cdot f(x)=\rho\left[\nabla\cdot\left(\frac{f(x)}{\rho}\right)+\frac{f(x)}{\rho^2}\cdot\nabla\rho\right]. \tag{2.17}$$

These relations may be substituted in the integral in Eq. (2.7), and a manipulation similar to that leading to Eq. (2.15) may be applied to each term. The only additional step is that each of the expressions multiplying $\nabla\rho$ in the second term on the right-hand sides of Eqs. (2.16) and (2.17) is brought outside the integral and evaluated at the point at which the gradient is being evaluated [Benz (1990)]. The results for the divergence of f at the position x^I of the I^{th} particle are

$$\nabla\cdot f(x^I)\approx\frac{1}{\rho^I}\sum_{J=1}^{N}m^J(f(x^I)-f(x^J))\cdot\nabla W(x-x^J,h), \tag{2.18}$$

based on Eq. (2.16), and

$$\nabla \cdot f(x^I) \approx -\rho^I \sum_{J=1}^{N} m^J \left(\frac{f(x^I)}{(\rho^I)^2} + \frac{f(x^J)}{(\rho^J)^2} \right) \cdot \nabla W(x - x^I, h), \tag{2.19}$$

based on Eq. (2.17). The rationale behind the use of these relations will be discussed in the next section.

2.2 Numerical algorithm

The only spatial gradients which must be evaluated in a standard Lagrangian finite-difference numerical algorithm are the stress divergence in the equations of motion

$$a = \frac{1}{\rho} \nabla \cdot \sigma, \tag{2.20}$$

where σ is the Cauchy stress tensor, and the velocity gradients in the strain-rate tensor,

$$\dot{\varepsilon}_{ij} = \frac{1}{2} \left(\frac{\partial V_i}{\partial x_j} + \frac{\partial V_j}{\partial x_i} \right), \tag{2.21}$$

and in the vorticity tensor

$$\omega_{ij} = \frac{1}{2} \left(\frac{\partial V_i}{\partial x_j} - \frac{\partial V_j}{\partial x_i} \right). \tag{2.22}$$

When indicial, rather than direct, notation is used the subscripts i and j refer to the spatial components in the x_1, x_2, and x_3 directions. Straightforward application of Eq. (2.15) to the equation of motion gives the acceleration of the I^{th} particle,

$$a_i^I = -\sum_{j=1}^{3} m^J \sum_{J=1}^{N} \frac{\sigma_{ij}^I}{\rho^I \rho^J} \frac{\partial W}{\partial x_j^I}. \tag{2.23}$$

Alternatively, Eq. (2.19) may be used, with the result

$$a_i^I = -\sum_{J=1}^{N} m^J \sum_{j=1}^{3} \left[\left(\frac{\sigma_{ij}}{\rho^2} \right)^I + \left(\frac{\sigma_{ij}}{\rho^2} \right)^J \right] \frac{\partial W}{\partial x_j^I}. \tag{2.24}$$

The latter relation has the advantage that the force on particle I due to particle J is the same as that on particle J due to particle I, so that strict momentum conservation is guaranteed. For the velocity gradient, an analogue of Eq. (2.15) yields

$$\left(\frac{\partial V_i}{\partial x_j} \right)^I = -\sum_{J=1}^{N} \frac{m^J}{\rho^J} V_i^J \frac{\partial W}{\partial x_j^I} \tag{2.25}$$

However, application of Eq. (2.18) yields

$$\left(\frac{\partial V_i}{\partial x_j} \right)^I = \frac{1}{\rho^I} \sum_{J=1}^{N} m^J (V_i^I - V_i^J) \frac{\partial W}{\partial x_j^J}. \tag{2.26}$$

The latter relation has the advantage that the contribution to the strain rate tensor from particles I and J is zero if their relative velocity is zero. In general, there are only minor differences between the regular forms, Eqs. (2.23) and (2.25), and the symmetric forms, Eqs. (2.24) and (2.26), except in special cases which can occur at boundaries.

Various schemes exist for advancing the solution in time, but a simple centered-difference scheme for the approximation of time derivatives will result in a numerical algorithm which differs from a standard Lagrangian finite-difference technique only in the approximations to the spatial derivatives described above. Since the equations of motion involve no time derivatives, all quantities are evaluated at the same time. Consequently, the equation of motion, Eq. (2.24), provides accelerations at time t^n from stresses and positions known at time t^n. The new velocities and positions can then be obtained from

$$V_i^{I,n+1/2} = V_i^{I,n-1/2} + \tfrac{1}{2}(\Delta t^{n+1/2} + \Delta t^{n-1/2}) a_i^{I,n} \tag{2.27}$$

and

$$x_i^{I,n-1} = x_i^{I,n} + \Delta t^{n+1/2} V_i^{I,n+1/2}. \tag{2.28}$$

The superscripts involving n denote the time at which the quantity is evaluated. The centered temporal difference scheme results in accelerations and positions being evaluated at integral times, while velocities are evaluated at half-integral times. Equations (2.27) and (2.28) allow the new positions at time t^{n+1} to be determined from accelerations at time t^n. The strain rates can then be determined from the velocity gradient. Proper time centering requires that the rates be evaluated at time $t^{n-1/2}$, so positions and densities at that time must be used in the kernel approximation for the velocity gradient. Quantities at half-integral times can be evaluated from expressions of the form

$$x_i^{I,n+1/2} = \tfrac{1}{2}(x_i^{I,n+1} + x_i^{I,n}). \tag{2.29}$$

The new density at time t^{n+1} can be determined directly from the kernel approximation, Eq. (2.14), resulting in

$$\rho(x) = \sum_{J=1}^{N} m^J W(x - x^J, h), \tag{2.30}$$

where all positions are evaluated at time t^{n-1}. However, Eq. (2.30) results in undesirable effects at boundaries. Figure 2 shows a graphical representation of the kernel density calculated from a set of equal masses with spacing h. The contribution from each mass point is represented by a curve which is an image of the kernel function. Thus, each point's mass

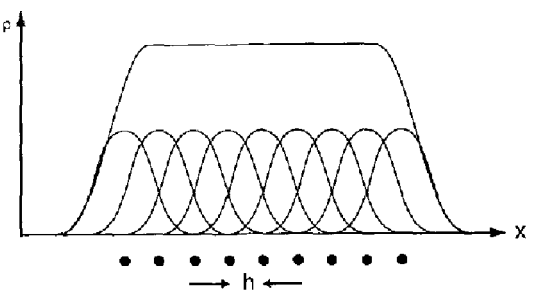

Fig. 2. Kernel density from equally spaced mass points

seems to be spread in space over a distance $2h$, which is in fact the basis of the 'smoothed particle' terminology. However, it is more valid to think of the particles as interpolation points rather than interacting masses. The density at any position is the sum of the contributions from all points, with only those within a distance $2h$ providing a non-zero contribution. For equal masses with an equal spacing of h, the density in the interior is independent of position. However, the boundary particle sees a contribution from points on only one side, rather than from both sides as in the interior, and the calculated density is less. Equation (2.30) thus results in boundary anomalies unless special boundary treatments are implemented. An alternative method is to solve the continuity equation

$$\frac{\dot{\rho}}{\rho} = -\nabla \cdot V = -\sum_{j=1}^{3} \frac{\partial V_j}{\partial x_j}. \tag{2.31}$$

Using Eq. (2.26) in a centered finite-difference temporal formulation of Eq. (2.31) results in

$$\rho^{I,n+1} = \rho^{I,n} - \Delta t^{n+1/2} \left\{ \sum_{J=1}^{N} m^J \sum_{j=1}^{3} (V_j^I - V_j^J) \frac{\partial W}{\partial x_j^I} \right\}^{n+1/2}. \tag{2.32}$$

This relation allows the initial density to be set to the desired value at each point, with density changes resulting only from relative motion between points. In practice, Eqs. (2.30) and (2.32) give identical results at interior points. The new densities at time t^{n+1} and the strain rates at time $t^{n+1/2}$ allow the equation of state to be evaluated at time t^{n+1}. Material strength is clearly included in the above formulation, since all components of the stress and strain rate tensors are treated. In fact, the equation of state can be completely arbitrary, especially when internal state variables are associated with each point. Given the Lagrangian nature of the points, tracking arbitrary internal state variables is a trivial process.

2.3 Artificial viscosity

Since the differential equations expressing conservation of mass, momentum, and energy apply only to regions of continuous flow, an artificial viscosity [von Neumann and Richtmyer (1950)] is required to smooth shocks into continuous steady waves and prevent the formation of mathematical discontinuities. The artificial viscous stress used in standard Lagrangian finite-difference methods [Swegle (1978)] is

$$Q = \rho b_1^2 \left(\frac{\dot{\rho}}{\rho}\right)^2 + \rho b_2 C \left(\frac{\dot{\rho}}{\rho}\right), \tag{2.33}$$

where b_1 and b_2 are constants with dimensions of length, and C is the sound speed. To produce a shock width consistent with the numerical resolution, the dimensional constants are scaled by a characteristic resolution length, l, which in SPH should be related to the smoothing length, h. The viscous stress can then be written in the form

$$Q = \rho B_1^2 l^2 \left(\frac{\dot{\rho}}{\rho}\right)^2 + \rho B_2 l C \left(\frac{\dot{\rho}}{\rho}\right), \tag{2.34}$$

hereafter referred to as the finite-difference artificial viscosity, where B_1 and B_2 are dimensionless coefficients, which in standard finite-difference methods usually have the values $B_1 = 2$, $B_2 = 0.1$. Typically, the artificial viscosity is used only in compression, and Q is set to zero on expansion. However, in certain cases, such as rarefaction shocks, it is necessary to turn the artificial viscosity on in expansion. A form of Eq. (2.34) which has the correct sign both in compression and expansion is

$$Q = \rho l \left(\frac{\dot{\rho}}{\rho}\right)\left(B_1^2 l \left|\frac{\dot{\rho}}{\rho}\right| + B_2 C\right). \tag{2.35}$$

The artificial viscosity is a mean stress which can be stored at each point and added to the stress tensor to form a total stress for use in the equations of motion. The equation of motion thus becomes

$$a_i^I = -\sum_{J=1}^{N} m^J \sum_{j=1}^{3} \left[\left(\frac{\sigma_{ij} - Q\delta_{ij}}{\rho^2}\right)^I + \left(\frac{\sigma_{ij} - Q\delta_{ij}}{\rho^2}\right)^J \right] \frac{\partial W}{\partial x_j^I}, \tag{2.36}$$

where $Q\delta_{ij}$ is subtracted from σ_{ij} since Q is positive in compression while σ_{ij} is positive in tension.

Previous SPH investigators have reported that the above form of the artificial viscosity is inadequate to prevent oscillations on the scale of the particle spacing, and an alternative SPH artificial viscosity formulation [Monaghan and Gingold (1983)] is used which takes the form of an interparticle stress given by

$$Q^{IJ} = \rho^2 \Pi^{IJ}, \tag{2.37}$$

where

$$\Pi^{IJ} = \frac{\alpha C^{IJ} \mu^{IJ} - \beta (\mu^{IJ})^2}{\rho^{IJ}}, \tag{2.38}$$

$$\mu^{IJ} = \frac{h \sum_{j=1}^{3} (V_j^I - V_j^J)(x_j^I - x_j^J)}{(|x^I - x^J|)^2 + \varepsilon h^2}, \tag{2.39}$$

$$C^{IJ} = \tfrac{1}{2}(C^I + C^J), \tag{2.40}$$

and

$$\rho^{IJ} = \frac{1}{2}(\rho^I + \rho^J). \tag{2.41}$$

The dimensions of Q^{IJ} are stress with the same sign convention as σ_{ij} (negative in compression), while Π^{IJ} has dimensions of stress divided by ρ^2, and μ^{IJ} has dimensions of velocity. Normally, Eq. (2.38) only applies if $\mu^{IJ} < 0$, so that particles I and J are approaching. Otherwise, $\Pi^{IJ} = 0$. A modification which provides the correct sign for Π^{IJ} regardless of the sign of μ^{IJ} and thus allows the viscosity to be used when particles are separating, is

$$\Pi^{IJ} = \frac{\mu^{IJ}(\alpha C^{IJ} + \beta |\mu^{IJ}|)}{\rho^{IJ}}. \tag{2.42}$$

With this form of the viscosity, since Q^{IJ} cannot be written as a viscous stress to be added to the normal equation of state stress of each material element, the equation of motion becomes

$$a_i^I = -\sum_{J=1}^{N} m^J \sum_{j=1}^{3} \left[\left(\frac{\sigma_{ij}}{\rho^2} \right)^I + \left(\frac{\sigma_{ij}}{\rho^2} \right)^J + \Pi^{IJ} \delta_{ij} \right] \frac{\partial W}{\partial x_j^I}. \tag{2.43}$$

Although the differences between the two forms seem minor, especially since μ^{IJ} would appear to be closely related to the volumetric strain rate, they have quite different properties.

2.4
Stability criterion

Explicit numerical solution methods such as the one described here must restrict the time step to a maximum value for the solution to remain stable. The CFL criterion [Courant, Friedrichs, and Lewy (1928)] essentially reduces to

$$\Delta t \leqq \frac{\Delta x}{C}, \tag{2.44}$$

where Δx is the smallest resolution length in the calculation. A stability criterion used for finite-difference methods [Swegle (1978)] takes the form

$$\Delta t \leqq \frac{k \Delta x}{B_2 C + 2B_1^2 |\dot{\rho}/\rho| \Delta x + \sqrt{(B_2 C + 2B_1^2 |\dot{\rho}/\rho| \Delta x)^2 + C^2}}, \tag{2.45}$$

where k is a safety factor usually equal to 0.9. This form includes modifications due to the artificial viscosity in the finite-difference form of Eq. (2.35). A stability criterion for the full SPH formulation including the viscosity in the SPH form of Eq. (2.38) has not been done, but a comparison of the coefficients in the two forms suggests that α corresponds to B_2, while β corresponds to B_1^2, at least on a dimensional basis.

2.5
Internal energy

Evolution of the internal energy is described by the relation

$$\rho \dot{E} = \sigma \cdot \dot{\varepsilon} + \dot{E}_Q \tag{2.46}$$

where E is the specific internal energy, σ is the stress tensor, $\dot{\varepsilon}$ is the strain rate tensor, given by Eq. (2.21), and E_Q is the contribution from the viscous stress. In finite-difference form this becomes

$$E^{n+1} = E^n + \left(\frac{\sigma \cdot \dot{\varepsilon} + \dot{E}_Q}{\rho/(\Delta t)} \right)^{n+1/2} \tag{2.47}$$

Since the components of σ and $\dot{\varepsilon}$ are known at each particle I, the term $\sigma \cdot \dot{\varepsilon}$ can be evaluated independently at each particle without the involvement of kernel sums. If the finite-difference artificial viscosity is used, then

$$\dot{E}_Q = -QI \cdot \dot{\varepsilon}, \tag{2.48}$$

where I is the unit tensor, since Q is simply an additive stress. However, if the SPH viscosity is used, then [Benz (1990)]

$$\dot{E}_Q = \frac{1}{2} \sum_{J=1}^{N} m^J \Pi^{IJ} \sum_{j=1}^{3} (V_j^I - V_j^J) \frac{\partial W}{\partial x_j^I}. \tag{2.49}$$

For an energy-independent equation of state, Eq. (2.47) may be evaluated directly once the stress has been determined. For an energy-dependent equation of state, simultaneous solution of the equations of state and energy evolution is frequently possible. Determining the new stress and internal energy at all points completes the calculations for a given cycle, allowing the time to be incremented, and the process to begin again.

2.6
Kernel function

In order to implement the SPH algorithm, the kernel function must be specified. Although numerous possibilities exist for the kernel function, one of the most widely used is the cubic b-spline kernel

$$W = \begin{cases} \dfrac{C}{h^D} \left[1 - \dfrac{3}{2} z^2 + \dfrac{3}{4} z^3 \right] & z < 1 \\ \dfrac{C}{4h^D} [2 - z]^3 & 1 \leqq z < 2 \\ 0 & z \geqq 2 \end{cases} \tag{2.50}$$

where

$$z = \frac{u}{h}, \tag{2.51}$$

u is the interparticle distance,

$$u = |\boldsymbol{x} - \boldsymbol{x}'|, \tag{2.52}$$

D is the dimension of the problem (1, 2, or 3), and the constant C is given by

$$C = \begin{cases} \dfrac{2}{3} & D = 1 \\ \dfrac{10}{7\pi} & D = 2 \\ \dfrac{1}{\pi} & D = 3. \end{cases} \tag{2.53}$$

The derivative of the kernel function is

$$\frac{\partial W(\boldsymbol{x} - \boldsymbol{x}')}{\partial x_j} = \frac{(x_j - x_j')}{u} \frac{\partial W}{\partial u} = -\frac{\partial W(\boldsymbol{x} - \boldsymbol{x}')}{\partial x_j'}, \tag{2.54}$$

where

$$\frac{\partial W}{\partial u}=\begin{cases}\dfrac{3C}{h^{D+1}}\left[-z+\dfrac{3}{4}z^2\right] & z<1\\[2ex] \dfrac{-3C}{4h^{D+1}}[2-z]^2 & 1\leqq z<2.\\[2ex] 0 & z\geqq 2\end{cases} \tag{2.55}$$

2.7 Variable smoothing length

In large deformation SPH calculations, it is clear that particle spacings may change dramatically from the initial configuration. In particular, if large expansions occur, particles may become separated by more than twice the smoothing length, h. In this case, the particles will no longer interact, and the calculation will break down. Thus, it is necessary to implement an algorithm to vary the smoothing length as strain accumulates. As indicated in Fig. 3, the smoothing length may be related to the particle size, or the volume occupied by the particle. If the particles are equally spaced with an inter-particle distance of h, the mass of the particle is related to its density and volume by

$$m=\rho h^D. \tag{2.56}$$

Thus, as the density of a fixed mass particle varies, one approach to implementing a variable smoothing length is

$$h\propto\left(\frac{m}{\rho}\right)^{1/D}. \tag{2.57}$$

This approach will not avoid difficulties in every situation, as illustrated in Fig. 4. Here a constant volume stretching is taking place, so that the particle separation is increasing in one direction and decreasing in the other, while the density remains constant. However, the variable smoothing length algorithm described below will remain essentially unchanged if Eq. (2.57) is replaced by a dependence on a different strain measure.

In the general case in which the smoothing length varies from particle to particle, symmetry and thus conservation of momentum is maintained if the smoothing length used for interactions between particles I and J is taken to be

$$h^{IJ}=\frac{(h^I+h^J)}{2}. \tag{2.58}$$

Variable smoothing is easily implemented in the equation of motion, since only quantities at time n are involved, and complete information at this time is available. With variable smoothing, Eq. (2.24) becomes

$$a_i^{I,n}=-\left\{\sum_{J=1}^{N}m^J\sum_{j=1}^{3}\left[\left(\frac{\sigma_{ij}}{\rho^2}\right)^I+\left(\frac{\sigma_{ij}}{\rho^2}\right)^J\right]\frac{\partial W(x^I-x^J,h^{IJ})}{\partial x_j^I}\right\}^n, \tag{2.59}$$

where

$$h^{I,n}=\left(\frac{m^I}{\rho^{I,n}}\right)^{1/D}. \tag{2.60}$$

Calculation of the new velocity gradient and density is less straightforward. If the smoothing length is constant in time, density is evolved according to the continuity equation, which in centered finite-difference form becomes

$$\left(\frac{\dot\rho}{\rho}\right)^{I,n-1/2}=\frac{(\rho^{I,n+1}-\rho^{I,n})/\Delta t^{n+1/2}}{\rho^{I,n+1/2}}=-\nabla\cdot V$$
$$=-\sum_{j=1}^{3}\left(\frac{\partial V_j}{\partial x_j}\right)^{I,n+1/2}, \tag{2.61}$$

where the velocity gradient is given by

$$\left(\frac{\partial V_i}{\partial x_j}\right)^{I,n+1/2}=\frac{1}{\rho^{I,n+1/2}}\left\{\sum_{J=1}^{N}m^J(V_i^I-V_i^J)\cdot\frac{\partial W(x^I-x^J,h^{IJ})}{\partial x_j^I}\right\}^{n+1/2}. \tag{2.62}$$

Inserting Eq. (2.62) in Eq. (2.61) and multiplying both sides by $\rho^{I,n+1/2}$ yields

$$\rho^{I,n+1}=\rho^{I,n}-\Delta t^{n+1/2}\left\{\sum_{J=1}^{N}m^J\sum_{j=1}^{3}(V_j^I-V_j^J)\frac{\partial W(x^I-x^J,h^{IJ})}{\partial x_j^I}\right\}^{n+1/2}. \tag{2.63}$$

Note that the expression for the velocity gradient requires the density at the new time, since

$$\rho^{I,n+1/2}=\tfrac{1}{2}(\rho^{I,n+1}+\rho^{I,n}). \tag{2.64}$$

However, the cancellation of the $\rho^{I,n+1/2}$ term allows the new density, which depends on the velocity gradient, to be calculated explicitly, rather than implicitly, which would be the case if terms on the right side of Eq. (2.63) contained the new density. In practice, the calculational procedure involves determination of the partial sums

$$\varphi_{ij}^{I,n+1/2}=\left\{\sum_{J=1}^{N}m^J(V_i^I-V_i^J)\frac{\partial W(x^I-x^J,h^{IJ})}{\partial x_j^I}\right\}^{n+1/2}. \tag{2.65}$$

which then allows the new density to be determined from

$$\rho^{I,n+1}=\rho^{I,n}-\Delta t^{n+1/2}\sum_{i=1}^{3}\varphi_{ii}^{I,n+1/2}, \tag{2.66}$$

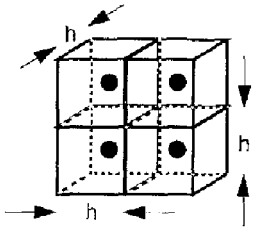

Fig. 3. Particle volume

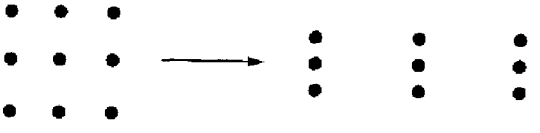

Fig. 4. Constant volume stretching deformation

while the velocity gradient is given by

$$\left(\frac{\partial V_i}{\partial x_j}\right)^{I,n+1/2} = \varphi_{ij}^{I,n+1/2} / \rho^{I,n+1/2}. \tag{2.67}$$

Unfortunately, in the general variable smoothing case, the smoothing length varies in time, so that the partial sums defined in Eq. (2.65) require the smoothing length at time $n + 1/2$, which is given by

$$h^{I,n+1/2} = \left(\frac{m^I}{\rho^{I,n+1/2}}\right)^{1/D} \tag{2.68}$$

in the present case of a density-based variable smoothing length, or in the more general case depends on some other strain measure. In either case, Eqs. (2.65) to (2.67) become highly implicit.

Several solution methods exist for this implicit set of equations. The most accurate and also the most time consuming would be to iterate, using the current value of h to calculate the new density, determining an improved value of h from Eq. (2.68), and recalculating the new density until convergence is achieved. A more expedient solution would simply be to use the old value of h, which basically assumes that the above iteration converges sufficiently in a single step. An alternate method would be to estimate the required value of h at $n + 1/2$ by the following procedure. Assume that the density increment does not change significantly from time $n - 1/2$ to time n, so that

$$\delta\rho^n = \rho^{n+1/2} - \rho^{n-1/2} \approx \delta\rho^{n-1/2} = \rho^n - \rho^{n-1}. \tag{2.69}$$

An estimated value of the density can then be found from

$$\rho_{\text{est}}^{n+1/2} = \tfrac{1}{2}(3\rho^n - \rho^{n-1}), \tag{2.70}$$

allowing the value of h at $n + 1/2$ required in Eqs. (2.65) to (2.67) to be estimated from

$$h_{\text{est}}^{I,n+1/2} = \left(\frac{m^I}{\rho_{\text{est}}^{I,n+1/2}}\right)^{1/D}. \tag{2.71}$$

3 Plane Wave on a spherical shell

The first test problem involves a plane acoustic wave incident on a hollow spherical elastic shell submerged in water. Analytic solutions are available for the response of the shell [Huang (1969), Zhang and Geers (1993)]. The first test involved a pure finite-element calculation using the two-dimensional axisymmetric mesh shown in Fig. 5. The left boundary is the cylindrical symmetry axis, and a pressure of roughly 20 atmospheres is applied to the top surface. This pressure was chosen to satisfy the acoustic approximation inherent in the analytic solution, and is so small that the relative motion between the water and the shell is essentially negligible during the time of the calculation. The right and bottom boundaries are placed far enough away from the shell that no wave reflections from them reach the shell during the time of the calculation. A close-up view of the mesh in the vicinity of the shell in shown in Fig. 6. The thickness of the shell is one-fiftieth of its radius, so that the individual elements in the shell cannot be detected. Comparisons of calculated and analytical results for the radial velocity at the top and bottom of the shell are shown in Fig. 7, for three different mesh resolutions. The coarse, regular, and fine calculations have 20, 50, and 125 elements along the half-circumference of the sphere. The calculations show excellent agreement with the analytic solution.

The second test involved a pure SPH calculation using the initial particle distribution shown in Fig. 8. The figure shows the initial particle distribution as well as the initial pressure and vertical velocity in the calculation. This is also an axisymmetric calculation with the particles reflected across the symmetry plane to generate the plot. Again, the thickness of the shell is so much less than its radius that individual

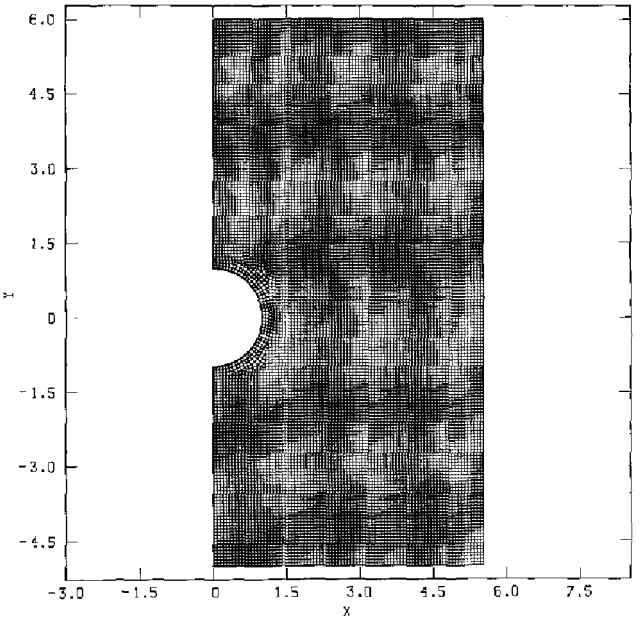

Fig. 5. Finite element mesh for the submerged sphere problem. Positions are in centimeters

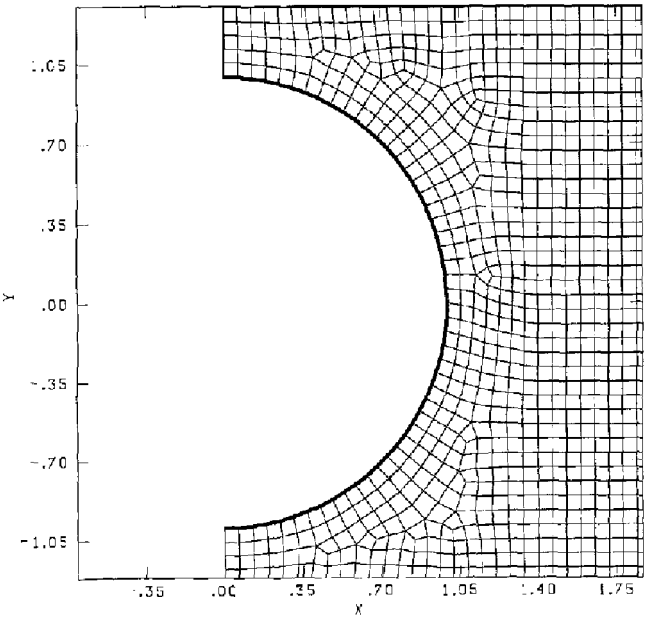

Fig. 6. Close-up of the finite-element mesh in the vicinity of the spherical shell

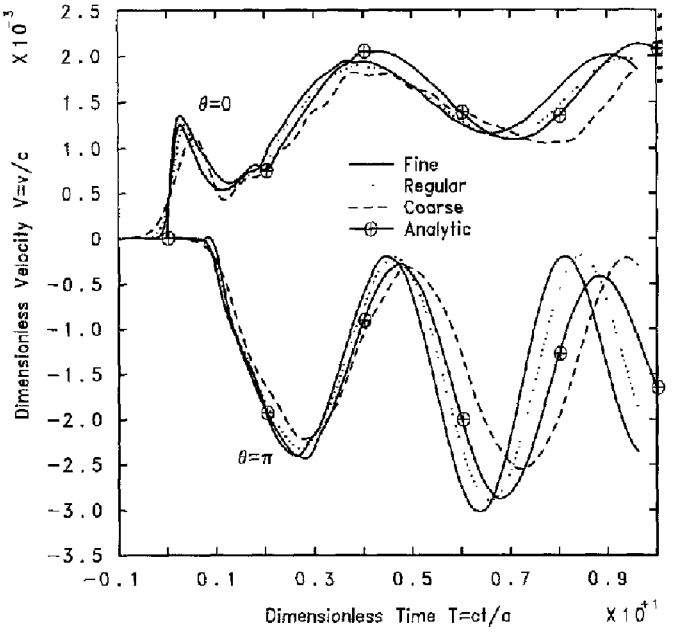

Fig. 7. Comparison of finite-element and analytical results for the velocity at the top ($\theta = 0$) and bottom ($\theta = \pi$) of the shell. Velocity and time are non-dimensionalized by the sound velocity in the water, c, and the radius, a, of the shell

particles in the shell cannot be detected, although the shell has uniform particle distribution with four particles through the shell thickness. In this calculation no attempt was made to match the positions of the water particles to the shell surface, but rather all particles in the water were placed on a regular lattice. No water particles were placed at a lattice positions which fell inside the outer diameter of the shell, resulting in the steps in the positions of the water particles next to the sphere surface. Although a smoother interface could easily have been constructed, it was of interest to see if this quick, albeit rather crude, placement could yield acceptable results. As shown in Fig. 9. the agreement between calculated and analytical results is again quite good.

4
Unde rwater bubble period and radius

The next test was to determine whether pure SPH could correctly predict the first period and maximum radius of the explosive products gas bubble resulting from the underwater detonation of an explosive charge. After detonation of the charge, the rapid expansion of the bubble and the inertia of the outwardly moving water cause the bubble to expand beyond the point of pressure equilibrium. After further expansion the higher pressure in the surrounding water reverses the motion and the bubble contracts. Again, equilibrium is overshot, and at the next minimum of the bubble size the gas

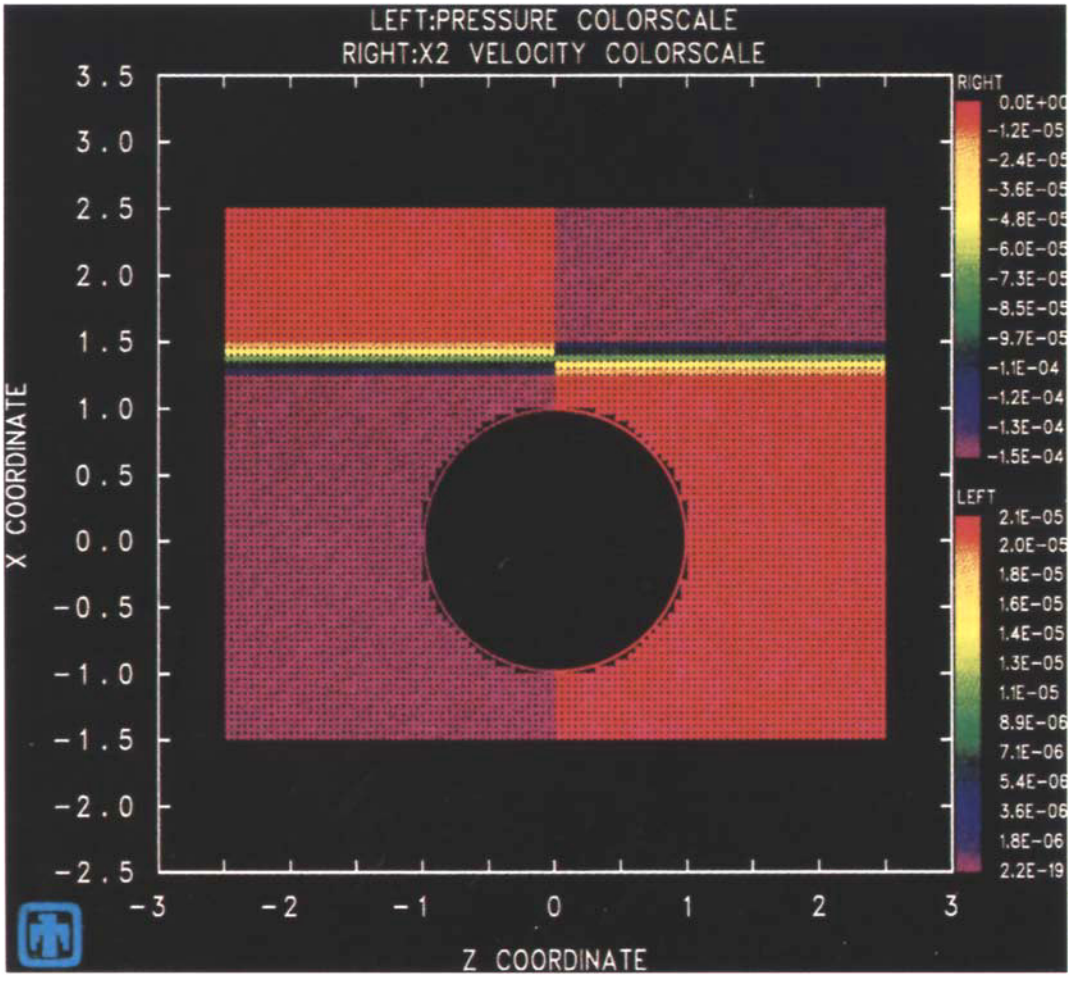

Fig. 8. Initial conditions for pressure and vertical particle velocity in the SPH calculation of the submerged sphere. Pressure is Mbar and velocity is cm/μ sec

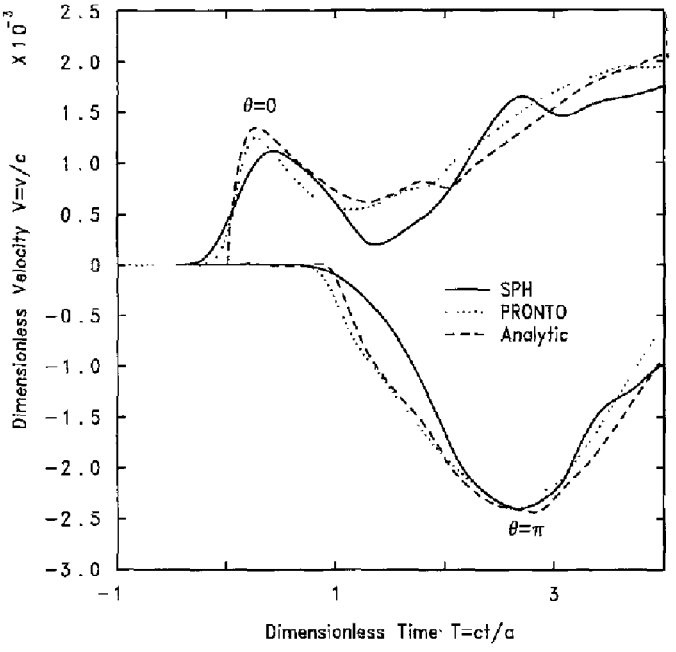

Fig. 9. Comparison of SPH and analytical results for the radial velocity at the top ($\theta = 0$) and bottom ($\theta = \pi$) of the shell. Velocity and time are non-dimensionalized by the sound velocity in the water, c, and the radius, a, of the shell

is recompressed to several hundred atmospheres. This forms a second 'explosion' and the process is repeated several times. Simple theories have been developed to predict the bubble period and maximum radius [Cole (1965)].

Pure SPH calculations were done to compare bubble period and radius with theory and also with results from other types of numerical methods. Comparison with other calculations is a more direct check of the SPH results than comparison with predictions of the simple theory, since the underlying physics and assumptions involved in the theory may differ from those in the calculations, and a specific calculation using a particular equation of state for the explosive and water may not necessarily agree with the theory. Two different calculations can be set up with identical conditions and material properties so that the only differences should be in the numerical solution methods. The SPH results were compared with results from the Lagrangian finite-difference wavecode TOODY [Swegle (1978)]. Although the SPH calculations were two-dimensional and axisymmetric, the deformations are too large for a gridded Lagrangian code, so the TOODY calculations were one-dimensional and spherically symmetric.

In order to keep the bubble period relatively short and to bound the ratio of the maximum bubble radius to the initial explosive radius, calculations were performed for the detonation of 1000 kg of TNT at a depth of 5000 m. The initial pressure in the surrounding water was set to the pressure at this depth, but rather than adding the acceleration of gravity and the variation of pressure with depth, the initial pressure in the water was about 0.5 kbar, independent of depth. Figure 10 shows SPH results for particle positions and pressures at times (from left to right and top to bottom) prior to detonation, at first bubble maximum, first bubble minimum, and second bubble maximum. The particles are reflected about the symmetry axis to produce the plot, with the color on the left side of the axis corresponding to type of particle (red for explosive, green for water), and the color on the right corresponding to a pressure color scale (pressure units in Mbar.) The boundaries are reflective and are only a few maximum bubble radii away from the detonation point in order to provide a close-up view of the particles in the gas bubble. The figure emphasizes the adaptive gridding provided by the variable smoothing length option in the SPH method. The explosive particles are initially considerably smaller than the water particles, but as they expand and their density increases, the size of the particle's interaction region increases so that they can keep in communication. Density in all calculations shown in this report is calculated by the kernel sum method, with boundary anomalies accounted for by multiplying all densities at all times by the ratio of the ambient density to the kernel sum density calculated at time zero.

Figure 11 shows a much larger calculation with the boundaries moved far enough away to have negligible effect on the first bubble period and maximum radius. In this calculation the position of the shock at the time of the first bubble maximum is clearly shown (upper right). The initial shock is just reflecting from the boundaries at the time of the first bubble minimum (lower left), and the outgoing pressure pulse produced at that time can clearly be seen interacting with the ingoing waves reflected from the boundary (lower right).

Comparisons of bubble size versus time for the two types of calculations for different mesh resolutions are shown in Fig. 12. In the figure legend, '2D SPH' refers to the SPH calculations, and '1D VNR' (von-Neumann Richtmyer difference method) refers to the TOODY calculations. As can be seen, resolution has an effect on the calculations. The two methods are in reasonable agreement, even though the SPH calculations are not truly spherically one dimensional. The simple theory predicts a maximum bubble radius of about 2 m, and a first period of about 16 ms, so the calculations are in general agreement with the simple theory, although the two numerical methods agree with each other better than with the theory.

5
Shallow explosion above a hollow cylinder

The next test involves the detonation of a shallow charge above a thin-walled aluminum pipe. The charge is 15 gm (2 mm/side) of pentolite at a depth of 7 cm, located 9 mm above a 46 cm (18 inch) diameter, 0.48 cm (0.19 inch) wall thickness pipe. The geometry is representative of a series of experiments known as IED cylinder tests [McClure (1993)]. The initial three-dimensional setup of the problem for a 3 foot long section of pipe is shown in Fig. 13. Gravity was not included and the initial pressure in the water is zero. The calculation demonstrates the full PRONTO capabilities for coupling different types of elements, since the explosive and nearby water are SPH (which is treated as simply another element type in PRONTO), the rest of the water is hex elements, and the pipe is shell elements. A close-up of the SPH region is shown in Fig. 14, which emphasizes the difference in the initial sizes of the SPH water particles and the SPH explosive particles.

Figure 15 shows the propagation of the pressure pulse due to the detonation of the explosive from the SPH region into

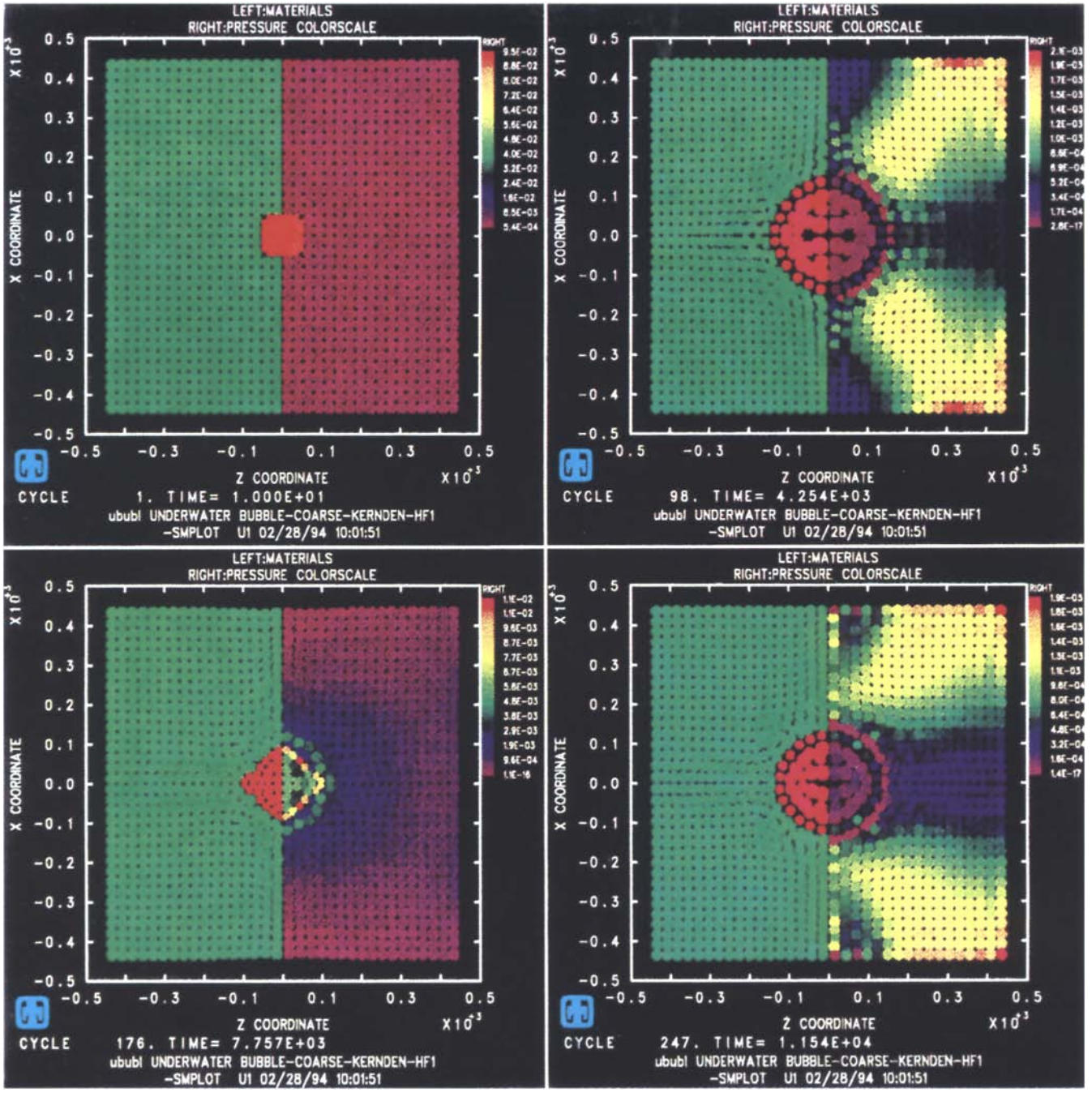

Fig. 10. Material and pressure plots for an underwater detonation with near boundaries. Pressure in Mbar

the surrounding finite-element water. The SPH particles and the shell elements are not shown in this figure. Figure 16 shows a series of plots of the material deformation at various times (indicated on the figure in microseconds). Again, the figure emphasizes the adaptive gridding of the variable smoothing length option in the SPH method as the size of the explosive particles increases while their density decreases. Although no quantitative comparisons were made with experiment because of unknowns in the experimental configuration, the calculations agree qualitatively with the deformations observed in the pipe in the tests, and demonstrate the feasibility of using PRONTO/SPH for coupled fluid-structure interactions.

6
Deep explosion beneath a flat plate

The final test involves the detonation of a deep charge beneath a flat steel plate. The plate is circular in shape, 70 inches in diameter and 1 inch thick, with a 1 foot diameter, 6 inch thick aluminum plug bolted into the center. The explosive charge is 10 gm of CH6, placed 5.5 inches below the center of the plate. The entire assembly is at a depth of 167 feet. This test is representative of a series of tests known as Seneca Lake [Thrun, Goertner, and Harris (1993)]. Figure 17 shows the initial three-dimensional mesh for the problem. The entire problem is represented by hexagonal finite elements, except for the explosive and water directly beneath the plate. This is

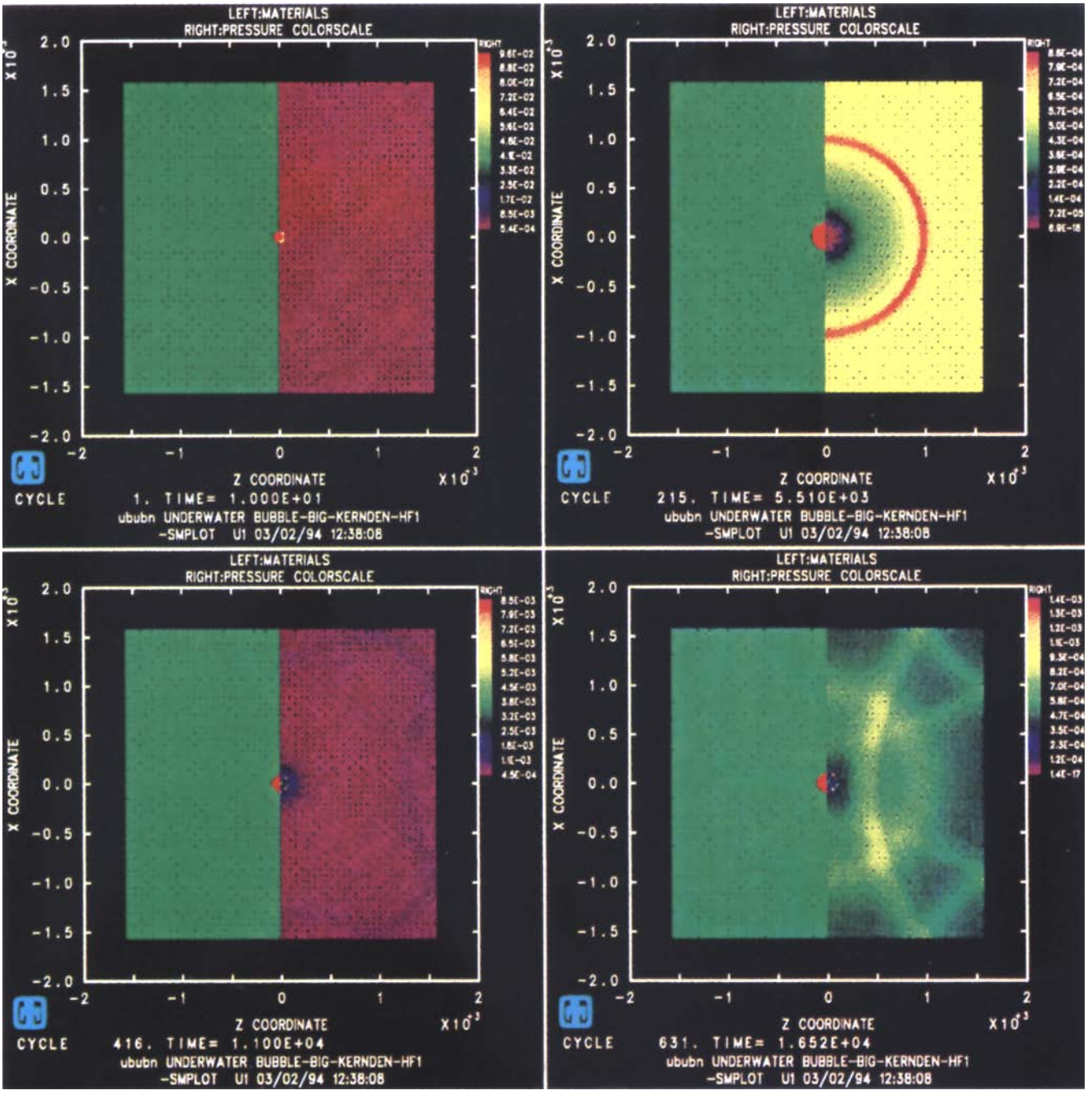

Fig. 11. Material and pressure plots for an underwater detonation with far boundaries. Pressure in Mbar

treated with SPH, shown in close-up in Fig. 18. For this problem gravity was included, and the initial pressure in the water was initialized to a depth-dependent value so that the pressure field in the water was in equilibrium with the acceleration of gravity. The initial pressure field in the water is shown in Fig. 19, with pressure units in Mbar. The initial pressure at the depth of the plate is about 6 bar. The water boundary at depths below the charge location was placed 2000 m away from the charge to preclude signals reflecting from the boundary back to the plate during the 15 ms duration of the event. The pressure was maintained by use of a no-displacement boundary condition at this location. To allow for vertical plate movement, an applied pressure boundary condition was used on the upper horizontal surfaces.

The propagation from the SPH region to the finite-element water of the initial pressure wave due to detonation of the explosive is shown in Fig. 20, at a time 0.9 ms after the detonation. Only the finite element water and not the SPH region or the metal plates is shown in the figure. A series of snapshots of the explosive bubble at various times during the calculation is shown in Fig. 21, in which the color of the SPH region is based on density. In the actual tests, the bubble is observed to expand until it begins to interact with the plate, and by 10 ms the upper portion of the bubble has risen to

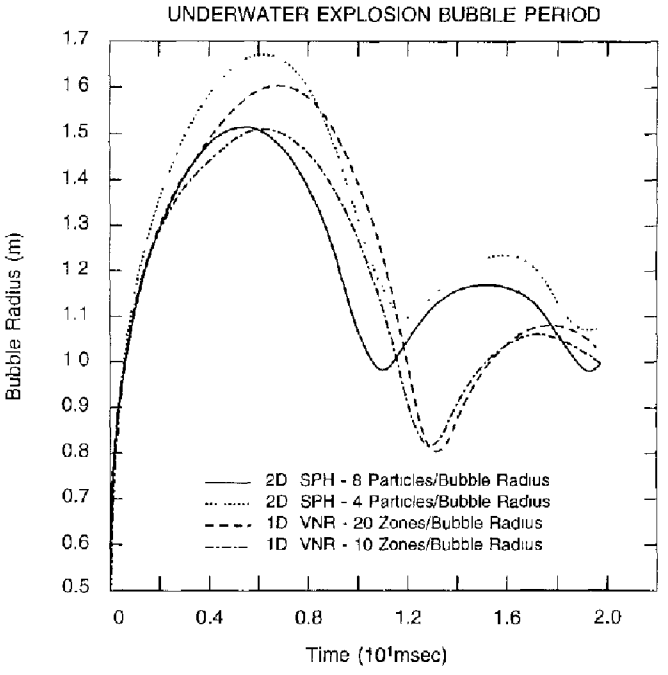

Fig. 12. Comparison of bubble size histories for 2D axisymmetric SPH calculations and 1D spherically symmetric TOODY (VNR) calculations

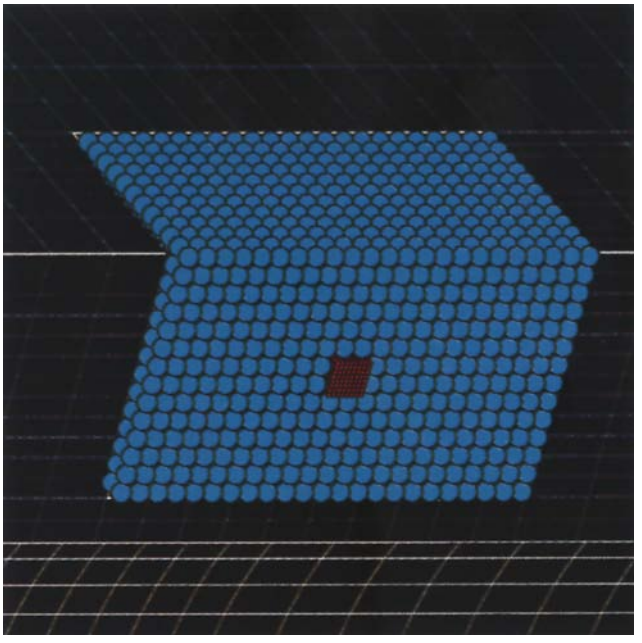

Fig. 14. Close-up of the SPH region for the submerged cylinder problem

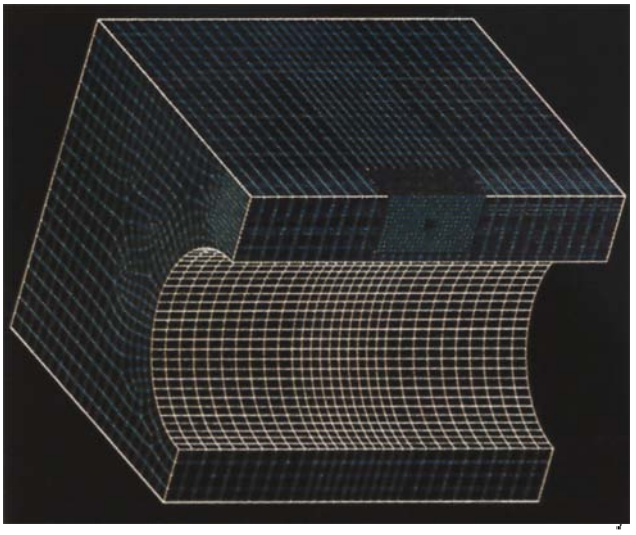

Fig. 13. Mesh for the submerged cylinder problem

contact and attach to the plate, producing a flat upper boundary. Around 12 ms the bubble begins to collapse from the bottom, producing a jet which impacts on the plate at about 15 ms. The figure shows that these events are not seen in the calculation. The bubble does not attach to the plate and begins to collapse uniformly near its original position. Also, the boundary between the SPH water and the finite element water shows an hourglass shape at late times due to the flow of the water apparently being too weak near the plate. This is indicative of excessive friction at the plate-water interface, which likely also affects the bubble motion in this region. However, it is clear that it is not reasonable to expect the calculations to be able to capture both the strong fluid-structure shock wave interactions present at early times in the calculation and also the late time effects due to acceleration of gravity and bubble buoyancy, without some special effort to mitigate numerical effects present not only in this method, but in most (all?) others as well. In the centimeter-gram-microsecond system of units which is most convenient for shock calculations, normal accelerations during an event are of the order of unity, while the acceleration of gravity is of order 10^{-9}. While most would consider a few percent to be reasonable accuracy in an explicit dynamics simulation of the type considered here, no one would expect accuracy in the 9^{th} significant digit. It is clear that numerical effects such as artificial viscosity, hourglass viscosity, and minor inaccuracies will swamp the late time phenomena seen in actual tests, and the ability to accurately model these phenomena in the same calculation which accurately models the early shock phenomena will require extensive method development and fine tuning of numerical artifacts. An additional concern is the amount of computer time required to reach such late times with an explicit dynamics calculation. The small spatial dimensions present in the problem limit the time step so that tens or hundreds of thousands of time steps may be required to reach the desired problem time, requiring tens or hundreds of hours of CPU time. Some sort of implicit method (with no explicit time step limitation) or perhaps an incompressible treatment might be more efficient for the intermediate stages of a problem such as this.

It might also be noted that the calculation shown above was done in three dimensions, even though the experiment is conceptually two-dimensional and axisymmetric. The

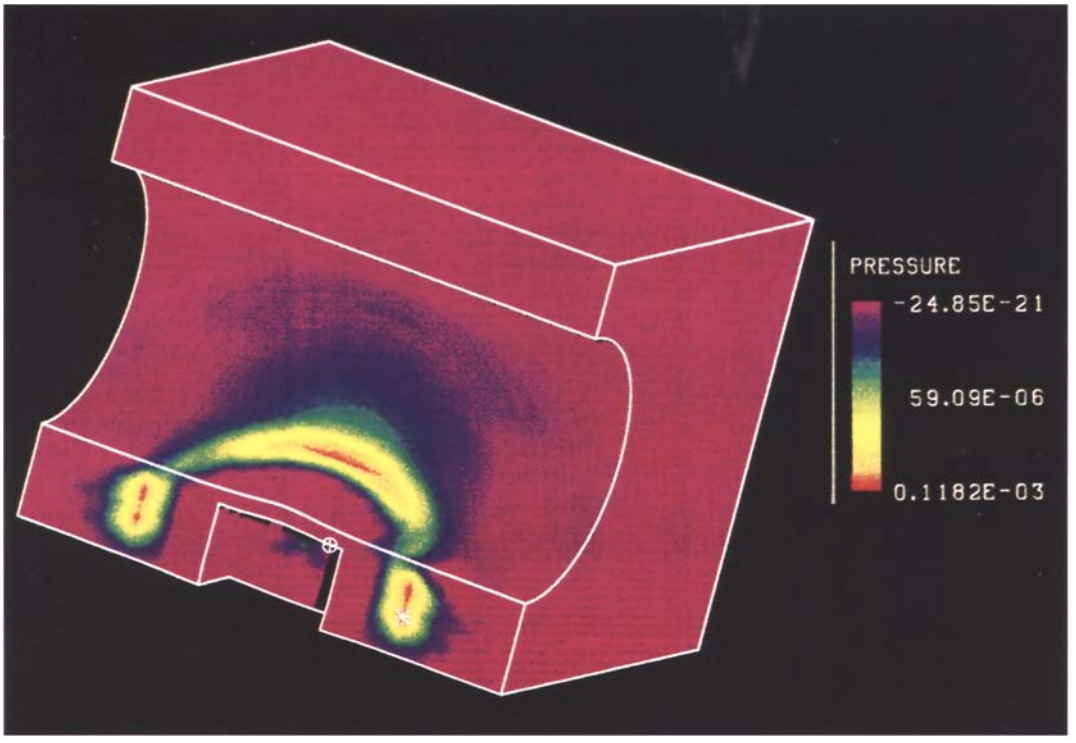

Fig. 15. Pressure pulse from detonation of the explosive charge. Pressure units in Mbar

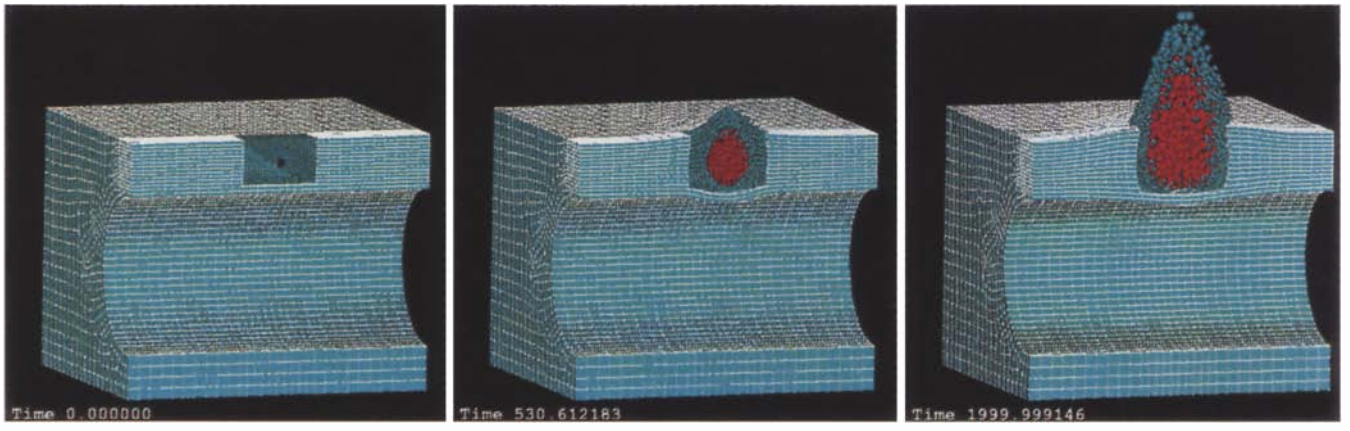

Fig. 16. Material deformation plots. Times in microseconds

axisymmetric option developed for PRONTO/SPH has been extensively tested and compared to analytic solutions in simple geometries where analytic solutions are known. The method clearly works and has been shown to produce correct results in these situations, as well as in the axisymmetric results shown previously. However, SPH has a peculiar difficulty in axisymmetric calculations which does not occur with gridded methods. Although the method is correct given a reasonable distribution of particles, in certain anomalous circumstances a single particle can get into trouble with the singularity at the symmetry axis. Since a single particle's density is proportional to radius due to the fact that a particle represents a torus of revolution in axisymmetry, particles which stray too near the axis can have their density and thus pressure increase to unreasonable levels. This would not occur with a gridded method, since even if a single element experienced a density increase as it neared the axis, the internal pressure in the element would cause it to expand, thereby reducing the pressure. However, a single particle has no degrees of freedom and cannot expand to reduce the density. Extreme pressures can thus be generated which destroy the calculation. An example is shown in Fig. 22, which shows the end-on impact of two cylinders. The material jets outward at the impact plane, whose normal is along the symmetry axis. The calculation proceeds normally until at late times a particle drifts too near the symmetry axis, producing a large pressure which then drives the other particles from its vicinity, effectively blowing a hole in the problem. This phenomenon does not occur in all axisymmetric calculations, but does prevent certain calculations from proceeding to completion.

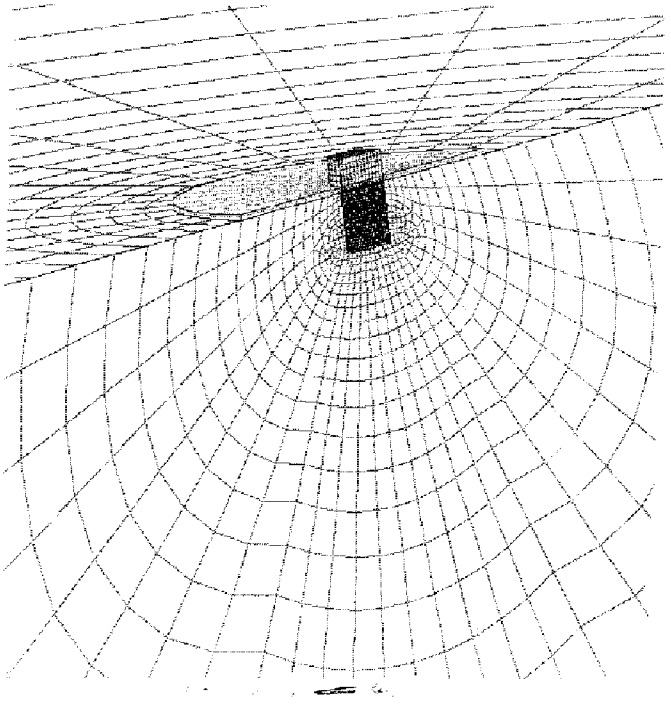

Fig. 17. Mesh for the flat plate problem

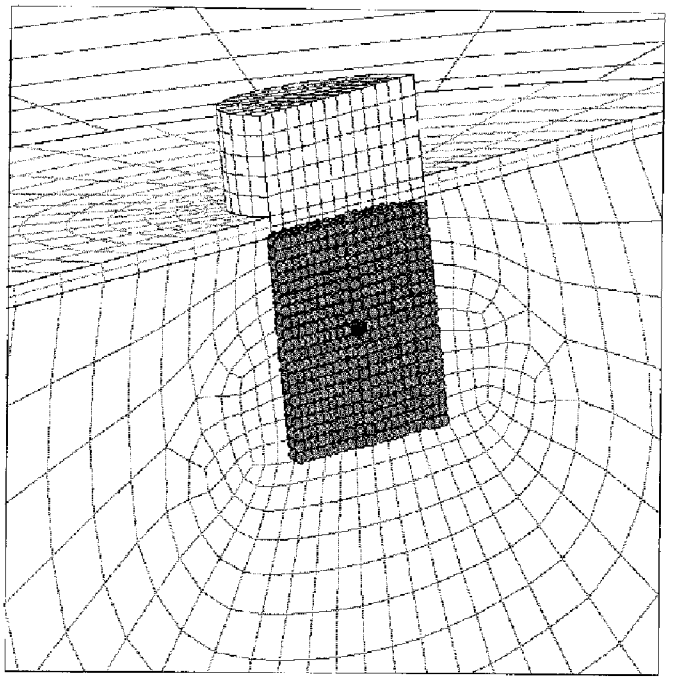

Fig. 18. Close-up of the SPH region for the flat plate problem

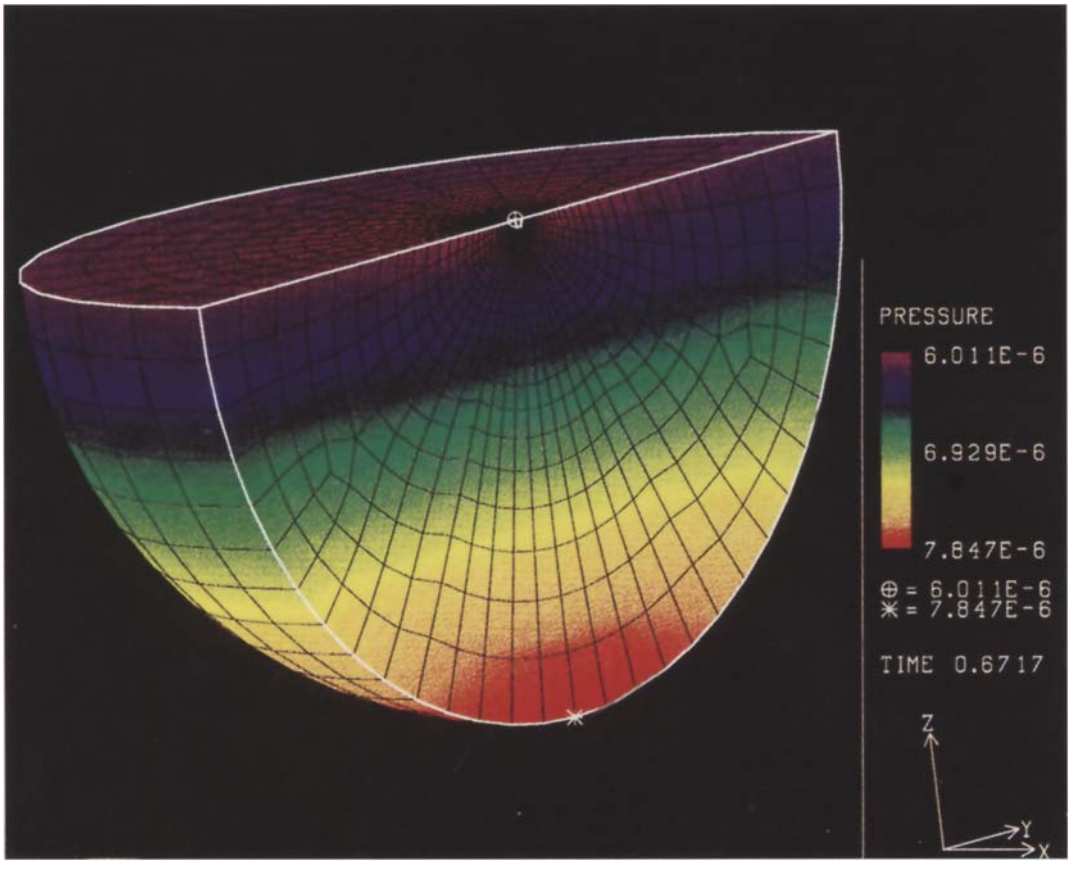

Fig. 19. Initial pressure field in the water in equilibrium with the acceleration of gravity. Pressure units in Mbar

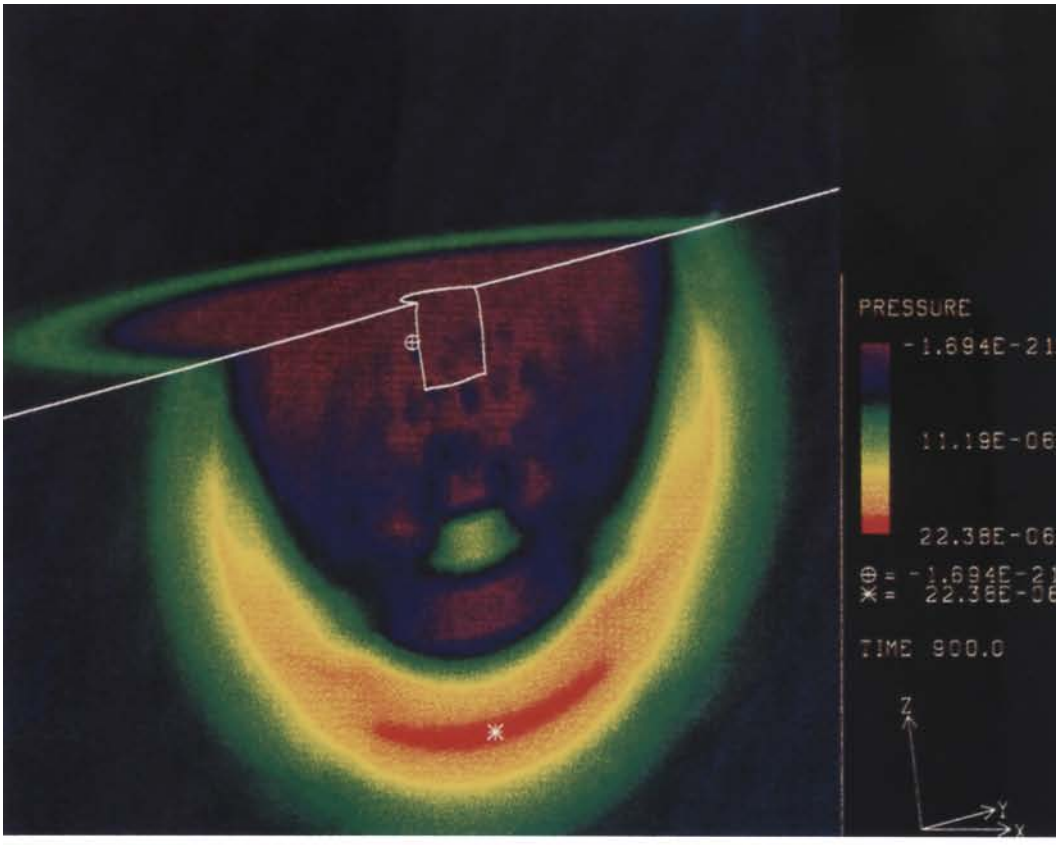

Fig. 20. Pressure pulse from detonation of the explosive charge. Pressure units in Mbar

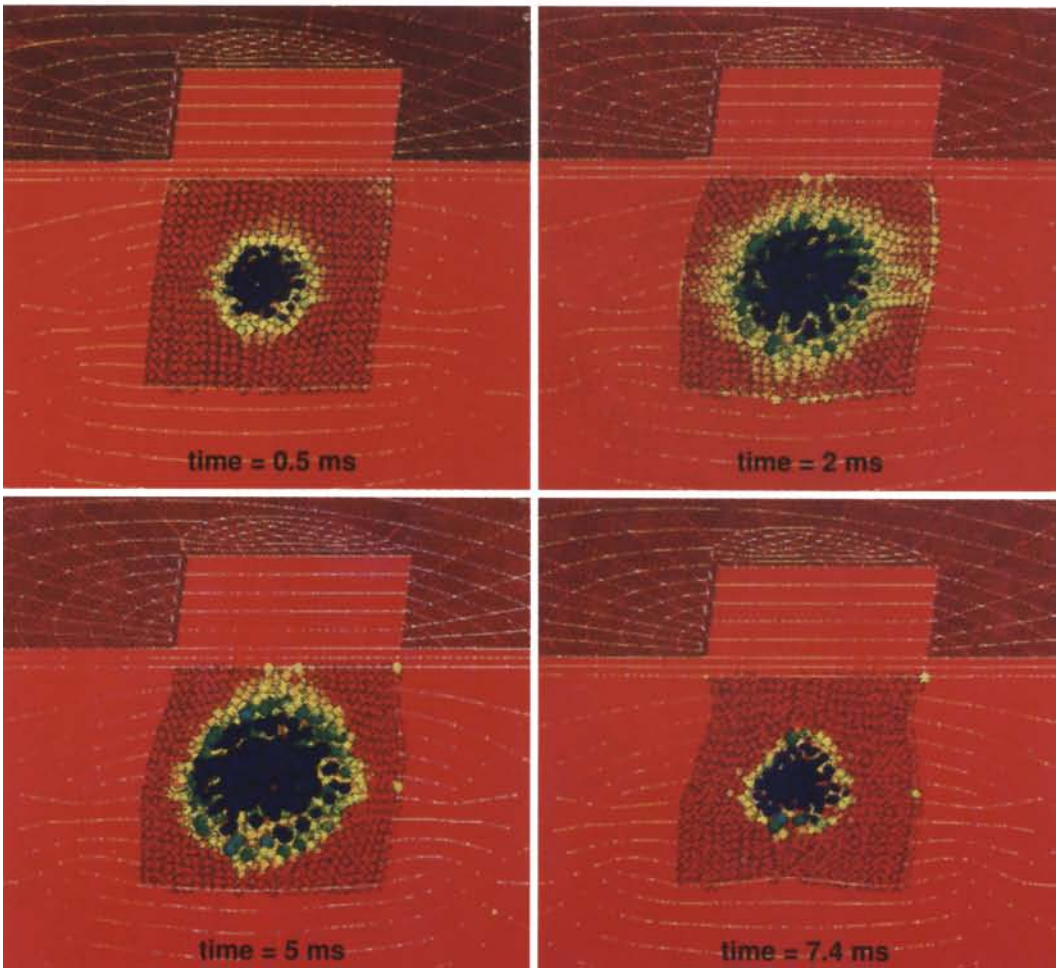

Fig. 21. Material deformation plots. Color based on density in the SPH region

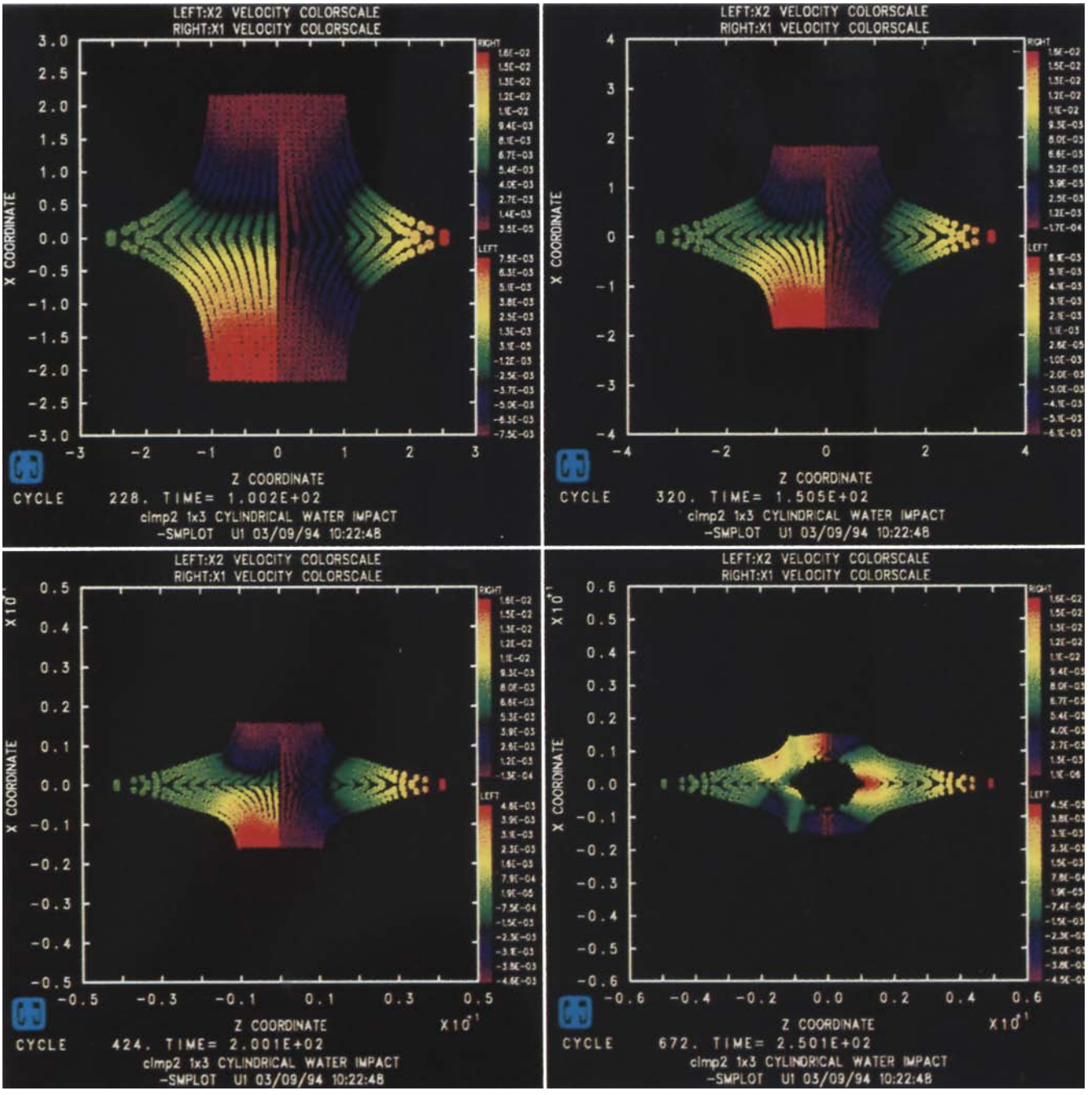

Fig. 22. End-on impact of two cylinders illustrating the axisymmetric singularity

7 Conclusion

Smoothed particle hydrodynamics (SPH) is a gridless Lagrangian technique which shows potential for detailed analysis of high deformation events which are not well handled at present by either Eulerian or standard Lagrangian techniques. In principle, the method should be able to overcome both the diffusion problems associated with Eulerian methods and the grid distortion associated with Lagrangian methods. The name 'smoothed particle hydrodynamics' is misleading, since the particles are actually interpolation points, and the method is not hydrodynamic, since inclusion of full stress and strain tensors is easily accomplished. The apparent strength of SPH is the calculation of spatial gradients by a kernel approximation method which does not require connectivity of the particles and should be able to treat arbitrary deformations. In the present study, the SPH algorithm has been subjected to detailed testing and analysis to determine its applicability to underwater explosion problems involving fluid-structure and shock-structure interactions.

The sample problems show that PRONTO/SPH is well-suited for transmission of loads from underwater explosions to nearby structures, including the permanent deformation of thin walled structures due to these explosions. However, it is clear

that it is not reasonable to expect the calculations to be able to capture both the strong fluid-structure shock wave interactions present at early times in the calculation and also the late time effects due to acceleration of gravity and bubble buoyancy. Numerical effects such as artificial viscosity, hourglass viscosity, and minor inaccuracies swamp these very late time phenomena which are due to physical forces and effects which are many orders of magnitude more subtle than those involved in the early parts of the event. The ability to accurately model these late-time phenomena in the same calculation which accurately models the early shock phenomena will require extensive method development and fine tuning of numerical artifacts. Also, the amount of computer time required to reach such late times with an explicit dynamics calculation is a major concern. The small spatial dimensions present in the problem limit the time step so that hundreds of thousands of steps may be required to reach the desired problem time, requiring tens or hundreds of hours of CPU time. An implicit method with no explicit time step limitation, or perhaps an incompressible treatments, might be more efficient for some parts of the problem. Although the current investigation has revealed areas in SPH (as well as most other numerical methods) that need improvement if late-time gravitational effects are to be modeled, the potential of the method in the area of large deformation Lagrangian calculations is very real.

References

Benz, W. 1990: Smooth Particle Hydrodynamics: A Review, in The Numerical Modeling of Stellar Pulsation, ed. J. R. Buchler (Dordrecht: Kluwer), 269

Cloutman, L. D. 1990: Basics of Smoothed Particle Hydrodynamics, Lawrence Livermore National Laboratory report UCRL-ID-103698

Cloutman, L. D. 1990: An Evaluation of Smoothed Particle Hydrodynamics, proceedings of The NEXT Free-Lagrange Conference, Jackson Lake Lodge, Moran, Wyoming, June 3–7

Cole, R. H. 1965: Under water Explosions, Dover Publications, 1965

Courant, R.; Friedrichs, K. O.; Lewy H. 1928: Math. Ann. 100: 32

Gingold, R. A.; Monaghan, J. J. 1982: Kernel Estimates as a Basis for General Particle Methods in Hydrodynamics, J. Comp. Phys. 46: 429–453

Huang, H. 1969: Transient Interaction of Plane Acoustic Waves with a Spherical Elastic Shell, J. Acoust. Soc. Amer. 45: 661–670

Lucy, L. B. 1977: A Numerical Approach to the Testing of the Fission Hypothesis, A. J. 82: 1013–1024

McClure, Charles, 1993: Preliminary Report on Explosive Field Tests in Support of the Hull Deformation/Rupture Study, NSWC Report NSWCDD/TN-93/94

Monaghan, J. J. 1982: Why Particle Methods Work, SIAM J. Sci. Stat. Comput. 3: 422–433

Monaghan, J. J. 1985: Particle Methods for Hydrodynamics, Comput. Phys. Rep. 3: 71–124

Monaghan, J. J. 1988: An Introduction to SPH, Comp. Phys. Comm. 48: 89–96

Monaghan, J. J.; Gingold, R. A. 1983: Shock Simulation by the Particle Method SPH, J. Comp. Phys. 52: 374–389

von Neumann, J.; Richtmyer, R. D. 1950: A Method for the Numerical Calculation of Hydrodynamic Shocks, J. Appl. Phys. 21: 232

Swegle, J. W. 1978: TOODY IV – A Computer Program for Two-Dimensional Wave Propagation, Sandia National Laboratories Report, SAND78-0552

Swegle, J. W.; Attaway, S. W.; Heinstein, M. W.; Mello, F. J.; Hicks, D. L. 1994: An Analysis of Smoothed Particle Hydrodynamics, Sandia National Laboratories Report, SAND93-2513

Swegle, J. W.; Hicks, D. L.; Attaway, S. W. 1995: Smoothed Particle Hydrodynamics Stability Analysis J. Comp. Phys. 116: 123–134

Taylor, L. M.; Flanagan, D. P. 1987: PRONTO 2D – A Two-Dimensional Transient Solid Dynamics Program, Sandia National Laboratories Report, SAND 86-0594

Thrun, Robert; John F. Goertner; Gregory S. Harris 1993: Underwater Explosion Bubble Collapse Against a Flat Plate. 1992 Seneca Lake Test Series Data Report, NSWC Report NSWCDD/TR-92/482

Zhang, Peizhen; Thomas L. Geers, 1993: Excitation of a fluid-filled, submerged spherical shell by a transient acoustic wave, J. Acoust. Soc. Amer. 93: 696–705